Aerospace Science and Technology 126 (2022) 107665

Contents lists available at ScienceDirect

Aerospace Science and Technology

www.elsevier.com/locate/aescte

Control of shock-wave/boundary-layer interaction using a backward-facing step

Jian Zhai [a,b,c,*], Chen-An Zhang [b], Fa-Min Wang [b], Wei-Wei Zhang [c]

[a] Chinese Aeronautical Establishment, Beijing 100029, People's Republic of China
[b] Institute of Mechanics, Chinese Academy of Sciences, Beijing 100190, People's Republic of China
[c] National Key Laboratory of Aerodynamic Design and Research, Northwestern Polytechnical University, Xi'an, Shaanxi 700072, People's Republic of China

ARTICLE INFO

Article history:
Received 3 June 2021
Received in revised form 14 May 2022
Accepted 25 May 2022
Available online 26 May 2022
Communicated by Yongle Du

Keywords:
Shock-wave/boundary-layer interaction
Backward-facing step
Flow separation
Hypersonic inlet

ABSTRACT

Flow separation induced by the shock-wave/boundary-layer interaction is detrimental to the performance of a hypersonic inlet. This paper develops a new method to control the shock-wave/boundary-layer interaction using a backward-facing step. The backward-facing step is placed on the shock-wave generator with a deflection angle of 14 deg. The shock-wave generator and a flat plate construct a simple hypersonic inlet. The control ability and mechanism are numerically studied using Reynolds Averaged Navier–Stokes equations at a freestream Mach number of 5. The results suggest that the backward-facing step can effectively suppress the flow separation. The reason is that the backward-facing step replaces the strong shock-wave in the baseline inlet with two weak ones. Consequently, the separation bubble in the controlled inlet is much smaller than that in the baseline inlet. Moreover, a parameter study is performed to analyze the effect of the design parameters of the backward-facing step on the control ability. The wave systems in the controlled inlet are classified into three types based on the results. However, only the effective wave system can suppress the shock-wave/boundary-layer interaction.

1. Introduction

A hypersonic inlet is a fundamental part of the scramjet. It captures and compresses the air in the freestream and provides compressed air for the combustor. However, flow separation induced by the shock-wave/boundary-layer interaction (SWBLI) may decrease the performance of the hypersonic inlet, such as mass-flow ratio and total pressure recovery coefficient [1–5]. If SWBLI is severe, the separation bubble may block the inlet and result in unstart [6–10]. Therefore, how to control SWBLI in the hypersonic inlet attracts much attention.

In recent years, various methods have been developed to control SWBLI. A widely used method is boundary-layer bleed and suction. Soltani et al. [11] used boundary-layer bleed to improve the stability margin of the inlet. The results indicated that if the bleed slot is located in a proper place, the subcritical performance and stability margin of the inlet can be enhanced. Huang et al. [12] indicated that the primary factors of the bleed systems are impingement angle, impingement distance, and backpressure at the plenum exit. He et al. [13] used a suction slot to control SWBLI. The results indicate that the control effect of the suction slot is significant. Zhang et al. [14] applied a novel unsteady pulsed suction technique to control the flow separations. The results indicated that the time-averaged suction flow rate plays a more crucial role than the excitation frequency. Wang et al. [15] used suction control to enhance the resistance backpressure characteristics. The results indicated that the most effective location is at the interaction of the shock train leading edge and the suction surface boundary layer. Zhang et al. [16] used suction to improve the performance of the diffuser. It indicated that sidewall suction is more effective to eliminate the low energy flow and stabilize the terminal shock wave. Sepahi-Younsi et al. [17] summarized recent developments of boundary layer suction. Although the boundary-layer bleed and suction can effectively control the SWBLI, it will cause mass flow loss and bring additional drag.

Another widely used method is using vortex generators [18–25]. Generally, the height of the vortex generators is smaller than the boundary-layer thickness. The underlying control mechanism is that the vortex generators mix the high-momentum fluid out of the boundary-layer and the low-momentum fluid in the boundary-layer. As a result, the mixed boundary-layer downstream of the vortex generators has a higher momentum to resist flow separation induced by SWBLI. However, this method also increases the aerodynamic drag [26,27].

* Corresponding author at: Chinese Aeronautical Establishment, Beijing 100029, People's Republic of China.
E-mail address: zhai_jian@mail.nwpu.edu.cn (J. Zhai).

https://doi.org/10.1016/j.ast.2022.107665
1270-9638/

Nomenclature

C_p	pressure coefficient
BFS	backward-facing step
BSW	shock-wave induced by the separation bubble
EWs	expansion waves
FML	forward Mach line
H	shape parameters
L	horizontal distance
L_{bubble}	length of the separation bubble
RML	rearward Mach line
SW	shock wave
SWBLI	shock-wave/boundary-layer interaction
t	thickness
θ	deflection angle of the BFS, momentum thickness
δ	thickness of the boundary-layer
δ^*	displacement thickness

Li [28] develops a method to decrease the aerodynamic drag and mass flow loss. The new method controls SWBLI using a backward-facing step (BFS). The BFS is placed on the flat plate and upstream of the impingement position of the incident shock-wave. The numerical results suggest that this method can reduce the height of the separation bubble but increase the length. Hence, the control ability of this method is limited. However, the advantages of using the BFS to control the SWBLI, smaller aerodynamic drag and less mass flow loss, are attractive to our group.

The BFS is a common aerodynamic configuration on supersonic vehicles and has been investigated for many years [29–31]. When the supersonic flow passes over the BFS, an expansion fan shows up at the step corner [32,33]. When the expansion fan interacts with a shock wave, it weakens the adverse pressure gradients caused by the shock wave. Therefore, if the expansion fan is placed at a proper location, the adverse pressure gradients which caused the SWBLI will be weakened, which means the SWBLI will be controlled.

This paper develops a new method using the BFS to control SWBLI. The aim is to improve the control ability of the BFS. In contrast to Ref. [28], this paper places the BFS on the shock-wave generator. The BFS replaces the strong shock-wave in the baseline inlet with weaker ones. Consequently, flow separation induced by SWBLI is suppressed. Section two introduces the controlled inlet and its ideal wave system. Section three presents numerical methods and verifications. Section four discusses the detailed control ability and mechanism of the BFS.

2. Inlet with the backward-facing step

Fig. 1 shows sketches of the baseline inlet [34]. It is a simplified hypersonic inlet and consists of a flat plate and a shock-wave generator with a deflection angle of 14 deg. At the Mach number of 5, the impingement position of the incident shock-wave (SW_0) is 350 mm from the leading edge of the flat plate. The boundary-layer upstream of the impingement position is turbulent. Hence, SW_0 interacts with the turbulent boundary-layer and generates $SWBLI_0$.

Fig. 2 shows the inlet controlled by the BFS and its ideal wave system. The BFS is colored by a solid purple line. There are two differences between the new BFS and the traditional BFS in Ref. [28]. The first difference is the place position: the traditional BFS is placed on the flat plate, while the new BFS is placed on the shock-wave generator. The second difference is the shape: the deflection

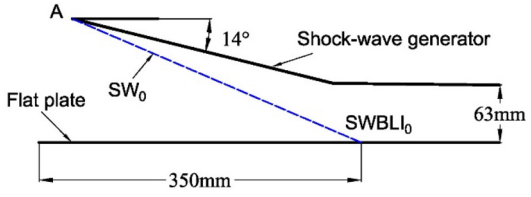

Fig. 1. Sketch of the baseline inlet [34].

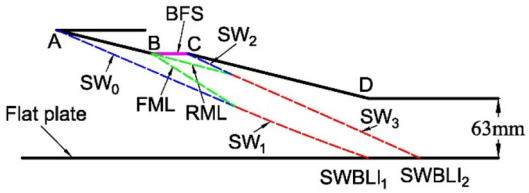

Fig. 2. Sketch of the controlled inlet and its ideal wave system. (For interpretation of the colors in the figure(s), the reader is referred to the web version of this article.)

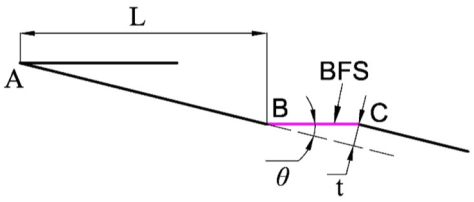

Fig. 3. Sketch of the parameters of the BFS.

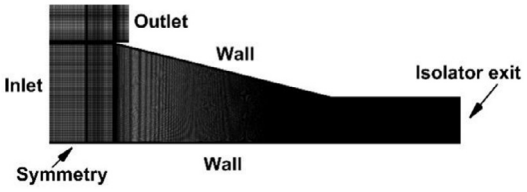

(a) The structured grid for computation

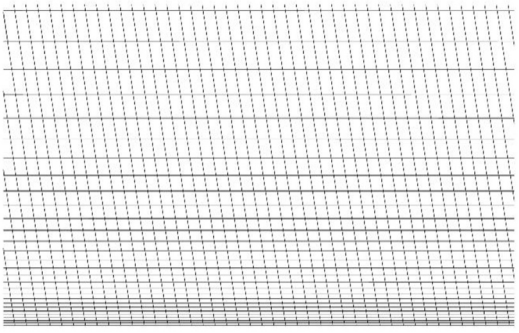

(b) The grid near the wall

Fig. 4. Grid for numerical simulation.

angle of the traditional BFS is 90 deg, which causes flow separation downstream of the BFS. Thus, the deflection angle of the new BFS is designed much smaller to avoid flow separation.

In Fig. 2, A is the leading edge of the shock-wave generator, B and C are the ending points of the BFS, and D is the end of the shock-wave generator. AB and BC construct a convex corner, while BC and CD construct a concave corner. According to the knowledge

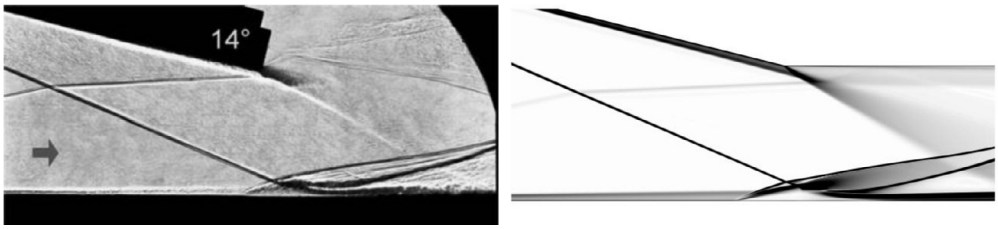

(a) Experimental result [34] (b) Numerical result

Fig. 5. Experimental and numerical schlieren images.

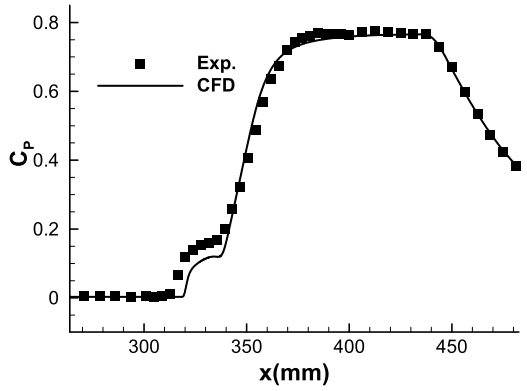

Fig. 6. Experimental and numerical pressure coefficient distributions on the flat plate.

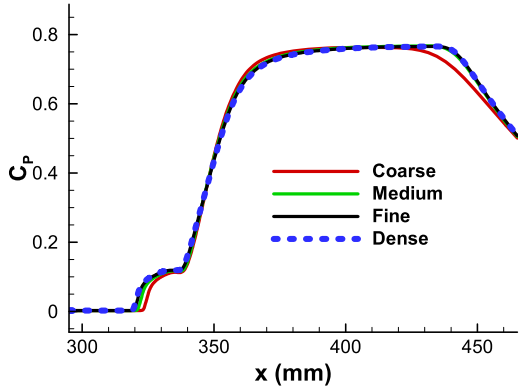

Fig. 7. Variation of pressure coefficient distribution on the flat plate.

of expansion waves and shock-waves in Ref. [35], when the supersonic flow passes over a convex corner, the expansion waves are in the shape of a fan and centered at the convex corner. The upstream boundary of the expansion waves is the forward Mach line (FML), while the downstream boundary of the expansion waves is the rearward Mach line (RML); they are both colored by dash green lines. In the control of the expansion waves, SW_0 changes into a weaker shock-wave SW_1. Consequently, the pressure downstream of SW_1 is smaller than that downstream of SW_0. Moreover, a new oblique shock-wave SW_2 appears in the flow-field due to the concave corner. SW_2 also changes into a weaker shock-wave SW_3 because of the expansion waves. SW_1 and SW_3 interact with the boundary-layer of the flat plate, respectively, and bring out $SWBLI_1$ and $SWBLI_2$. Because SW_1 and SW_3 are weaker than SW_0, $SWBLI_1$ and $SWBLI_2$ are also weaker than $SWBLI_0$.

Fig. 3 shows the sketch of the parameters of the BFS, including the horizontal distance (L) between A and B, the thickness (t), and the deflection angle (θ) of the BFS. The parameters of the BFS in Fig. 3 are $L = 26\delta$, $\theta = 14$ deg, $t = 0.8\delta$ (δ is the thickness of the boundary-layer at the position of 266 mm from the leading edge of the flat plate, $\delta = 3.8$ mm). Table 1 shows the parameters of the BFS in the parameter study.

Table 1
Parameters of the BFS in the parameter study.

L/δ	t/δ	θ (deg)
13, 26, 39, 52	0.8	14
26	0.3, 0.8, 1.6, 2.4	14
26	0.8	3, 7, 14, 30, 90

3. Numerical methodology

3.1. Numerical method

The numerical results are calculated using the compressible Reynolds-averaged Navier-Stokes (RANS) and Euler equations, respectively. A cell-centered finite volume method is used to solve the governing equations. The lower–upper symmetric Gauss-Seidel scheme (LU-SGS) [36] is used to perform temporal integration. Whereas a second-order, Roe's scheme [37] in conjunction with the Monotone Upwind Scheme for Conservation Laws (MUSCL) interpolation method [38] is used to discretize the inviscid fluxes. The viscous fluxes are discretized using the central difference method. The viscous flow is assumed to be fully turbulent, and the turbulent quantities are calculated using the shear-stress transport (SST) model [39] because previous studies suggest that this model can give reliable flow-filed of SWBLI [40,41]. The viscosity coefficient and thermal conductivity are both calculated using Sutherland's law [35]. A calorically perfect gas model is assumed; its specific heat ratio is 1.4.

Fig. 4 (a) shows a structured grid used for numerical simulation. The freestream Mach number is 5, the pressure is 4008.5 Pa, the temperature is 68.3 K, and the unit Reynolds number of the freestream is 3.7×10^6/m, which are calculated from the wind tunnel experiment data in Ref. [34]. For viscous simulations, the wall has a constant temperature of 300 K, and y+ near the wall is below one. The grid near the wall is shown in Fig. 4 (b). Moreover, the extrapolation boundary condition is imposed on the isolator exit.

3.2. Numerical validation

To verify the effectiveness of RANS equations, this paper compares the numerical result with the experimental result in Ref. [34]. Figs. 5 (a) and (b) show the experimental and numerical schlieren images, respectively. Fig. 6 shows the experimental and numerical pressure coefficient distributions on the flat plate. The results suggest that the numerical and experimental results agree well. So, the numerical method is reliable.

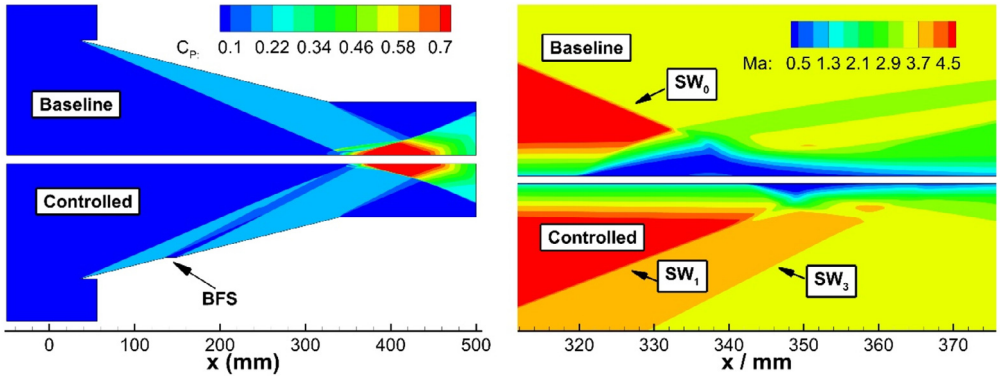

(a) Flow-filed of the inlets (b) Mach contours around the interaction region

Fig. 8. Numerical results of the baseline and controlled inlet.

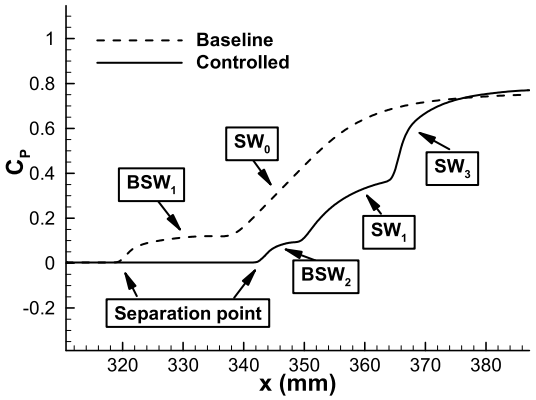

Fig. 9. Pressure coefficient distributions around SWBLIs.

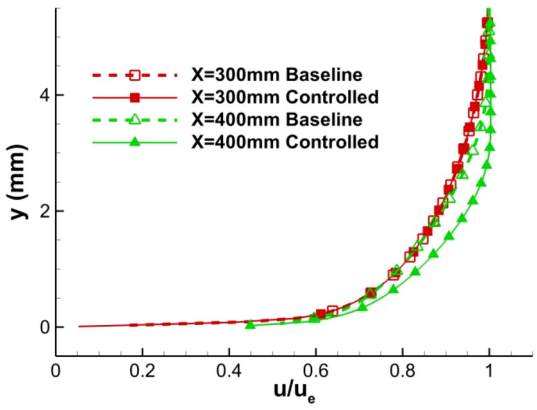

Fig. 10. Velocity profiles at $x = 300$ and 400 mm on the flat plate.

3.3. Grid convergence study

A grid convergence study for the controlled inlet is carried out using the RANS equations. Four grids (coarse, medium, fine, and dense) are used. They contain about 0.1, 0.2, 0.4, and 0.8 million nodes, respectively. Fig. 7 shows the variation of the pressure on the flat plate. The results calculated by the fine and dense grids are almost the same as each other. Hence, fine grids give reliable results. Thus, the fine grid is used for the subsequent numerical simulation to ensure accuracy and save the computing resources.

4. Results and discussion

4.1. Control effect

Fig. 8 shows the numerical results of the baseline and controlled inlets. The parameters of the BFS are $L = 26\delta$, $\theta = 14$ deg, $t = 0.8\delta$. In contrast to the baseline inlet, there is an additional low-pressure zone in the controlled inlet, as shown in Fig. 8 (a). The low-pressure zone is caused by the expansion waves induced by the BFS. Due to the expansion waves, the strong shock-wave

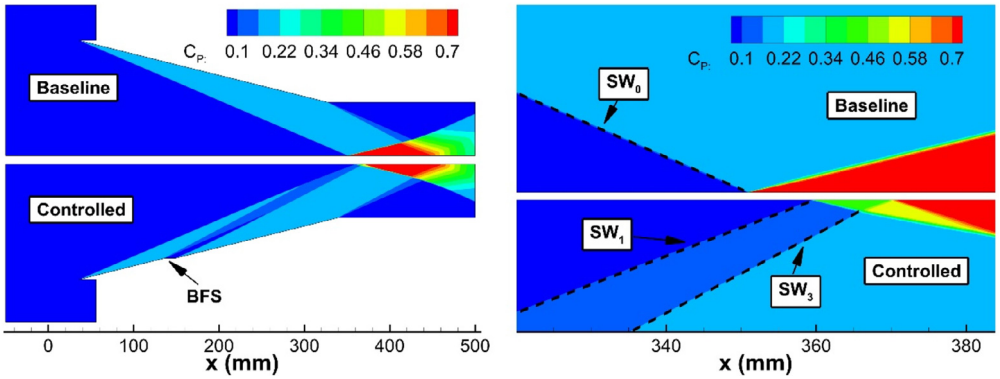

(a) Flow-fields of the inlets (b) Flow-fields around the interaction region

Fig. 11. Inviscid pressure coefficient contours of the baseline and controlled inlet.

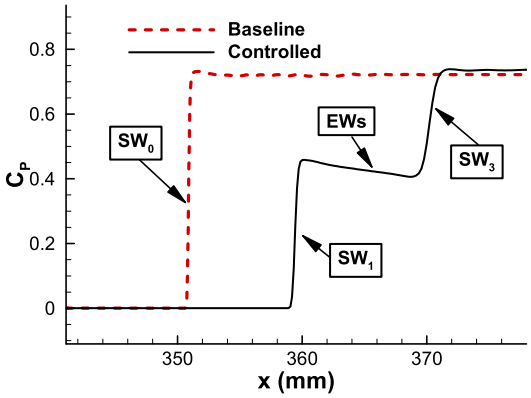

Fig. 12. Inviscid pressure coefficient distributions on the flat plate.

SW_0 in the baseline inlet is replaced by two weaker shock-wave SW_1 and SW_3, as shown in Fig. 8 (b). Consequently, the large separation bubble becomes a small one. The lengths of the separation bubbles are 31.2 and 11.7 mm, respectively, while the heights are 4.4 and 1.2 mm, respectively. Therefore, in control of the BFS, the length and height of the separation bubble are reduced by 62.5% and 72.7%, respectively, which means the volume of the small bubble is reduced by 90% of that of the larger bubble. It indicates that the BFS can effectively control SWBLI, and the control ability is better than that of the traditional BFS in Ref. [28].

Fig. 9 shows the pressure coefficient distributions around SWBLIs. The distributions suggest that the separation point moves downstream in control of the BFS. Although the pressure upstream of the separation points correspond with each other, those downstream of the separation points are different. In the baseline inlet, the pressure downstream of the separation point jumps twice. The first jump is caused by the shock-wave induced by the large separation bubble (BSW_1), while the second jump is caused by SW_0. In contrast, in the controlled inlet, the pressure downstream of the separation point jumps three times. The first jump is caused by the shock-wave induced by the small separation bubble (BSW_2), and the second and third jumps are caused by SW_1 and SW_3. The pressure jumps caused by SW_1 and SW_3 are much smaller than those caused by SW_0, which means SW_1 and SW_3 are weaker than SW_0.

4.2. Control mechanism

Fig. 10 shows the velocity profiles at $x = 300$ and 400 mm on the flat plate, $x = 300$ mm is upstream of the SWBLI, while $x = 400$ mm is downstream of the SWBLI. As can be seen, the velocity profiles at $x = 300$ mm are the same, which means the BFS does not affect the boundary-layer upstream of the SWBLI. However, the velocity profiles at $x = 400$ mm are different. The one in the controlled inlet is fuller than that in the baseline inlet. Table 2 shows integral parameters of the boundary layer at $x = 400$ mm. It suggests that the displacement thickness (δ^*) and momentum thickness (θ) in the controlled inlet are smaller than those in the baseline inlet, and the shape parameters (H) are almost the same. The above results indicate that the boundary layer is more difficult to separate under the control of the BFS.

Table 2
Integral parameters of the boundary layer at $x = 400$ mm.

	δ^* (mm)	θ (mm)	H
baseline	1.27	0.31	4.09
controlled	0.87	0.20	4.35

Souverein [42] indicates that the length of the separation bubble induced by SWBLI depends on two factors, including the thickness of the upstream boundary-layer and the pressure jump imposed by the shock-wave. The result in Fig. 10 shows that the boundary-layer thicknesses upstream of the SWBLI are identical, which means the control mechanism of the BFS is not by changing the thickness of the upstream boundary-layer.

According to the assumption in Ref. [42], the pressure jump induced by shock-wave equals the inviscid value. Hence, it is obtained using the Euler equations in this paper. Fig. 11 shows the inviscid pressure coefficient distributions of the inlets. The results suggest that the pressure downstream of SW_1 is smaller than that downstream of SW_0, while that downstream of SW_3 is almost the

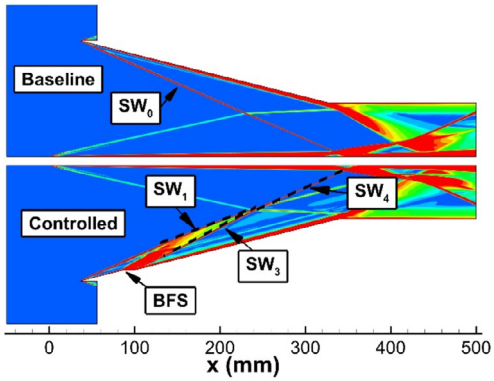

(a) Schlieren image when L=13δ

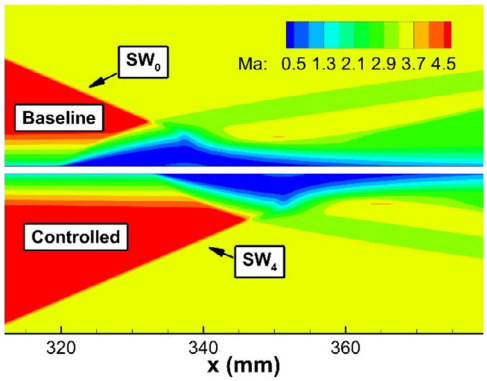

(b) Mach contours when L=13δ

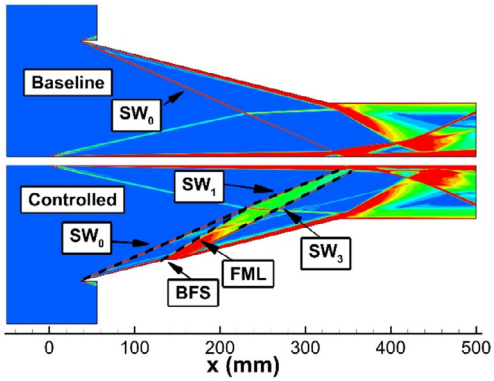

(c) Schlieren image when L=26δ

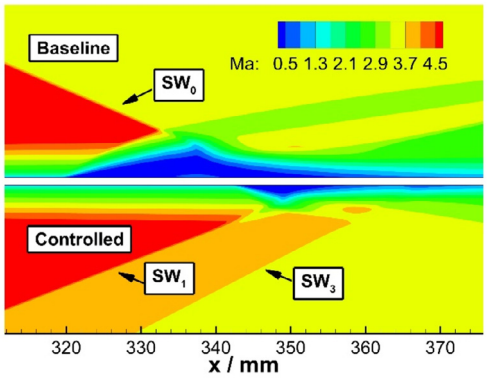

(d) Mach contours when L=26δ

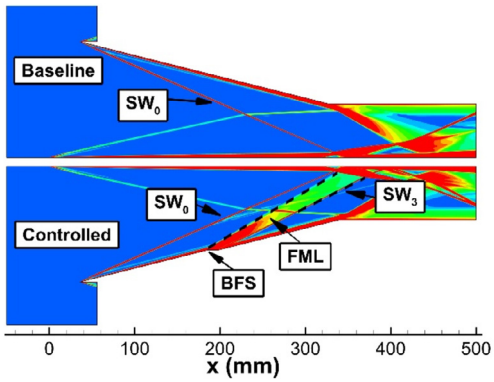

(e) Schlieren image when L=39δ

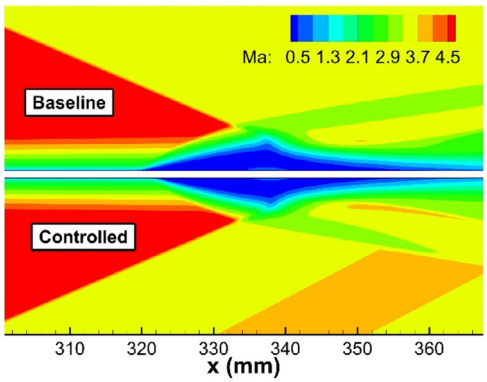

(f) Mach contours when L=39δ

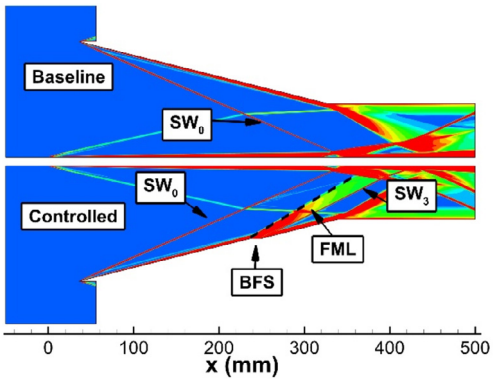

(g) Schlieren image when L=52δ

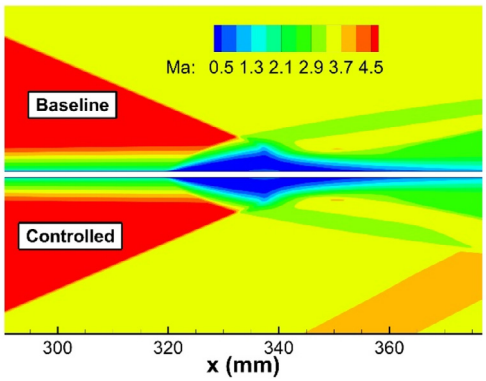

(h) Mach contours when L=52δ

Fig. 13. Effect of L on flow-fields of the inlets.

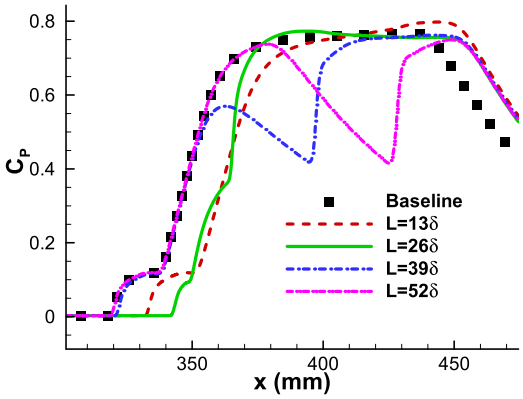

Fig. 14. Effect of L on the pressure coefficient distribution on the flat plate.

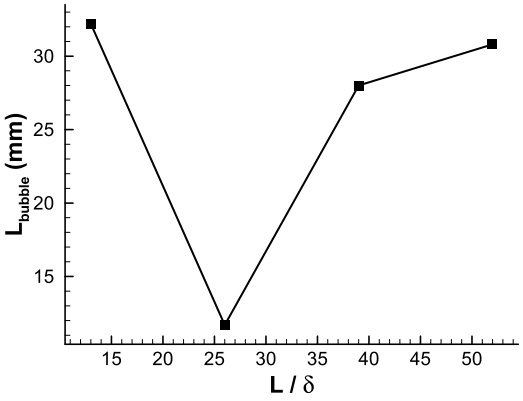

Fig. 15. Effect of L on the length of the separation bubble.

same as that downstream of SW_0. It indicates that the pressure jumps induced by SW_1 and SW_3 are smaller than that induced by SW_0.

Fig. 12 shows the inviscid pressure coefficient distribution on the flat plate. The pressure jumps induced by SW_1 and SW_3 are 65% and 44% of that induced by SW_0. Consequently, the control mechanism of the BFS is decreasing the pressure jump induced by the incident shock-wave to weaken the flow separation.

4.3. Parameter study

This section studies the effect of the design parameters of the BFS on SWBLI, including the horizontal distance (L) between A and B, the thickness (t), and the deflection angle (θ) of the BFS.

4.3.1. Horizontal distance (L) between A and B

Fig. 13 shows the effect of L on flow-fields of the inlets. Fig. 13 (a), (c), (e) and (g) show the schlieren images, while Fig. 13 (b), (d), (f) and (h) shows the Mach contours around flow separation. When $L = 13\delta$, SW_1 and SW_3 interact and generate SW_4, as shown in Fig. 13 (a). Although the separation bubble induced by SW_4 moves downstream, its size nearly equals that in the baseline inlet, as shown in Fig. 13 (b), which means the BFS is ineffective. When $L = 26\delta$, SW_1 and SW_3 interact with the boundary-layer of the flat plate, respectively, as shown in Fig. 13 (c). However, only SW_1 induces flow separation, and the separation bubble is much smaller than that in the baseline inlet, as shown in Fig. 13 (d). When $L = 39\delta$, FML induced by the BFS interacts with SW_0 on the flat plate, as shown in Fig. 13 (e), which means the effect of the BFS on SW_0 is tiny. Consequently, the separation bubble is nearly unchanged by the BFS, as shown in Fig. 13 (f). When $L = 52\delta$, FML does not interact with SW_0 at all, as shown in Fig. 13 (g), and the separation bubble in the controlled inlet is the same as that in the baseline inlet, as shown in Fig. 13 (h). It indicates the BFS is ineffective.

Fig. 14 shows the effect of L on the pressure coefficient distribution on the flat plate. When $L = 13\delta$, the pressure coefficient distribution in the controlled inlet is similar to that in the baseline inlet. It indicates that when $L = 13\delta$, the BFS can not decrease the pressure jump. When $L = 26\delta$, the pressure on the flat plate jump three times, and every jump is relatively small. When $L = 39$ and 52δ, the beginning positions of pressure jumps are almost the same as that of the baseline inlet, and the pressure coefficients decrease at $x = 361$ and 379 mm, then increase at $x = 395$ and 425 mm. The reason is that the pressure is decreased by the expansion waves and increased by SW_3.

Fig. 15 shows the effect of L on the length of the separation bubble (L_{bubble}). The results suggest that the length of the separation bubble decrease firstly and then increase. It indicates that the BFS can effectively control SWBLI when L is in a proper range. Thus, if L is too large or too small, the control effect is weak or even ineffective.

4.3.2. Thickness, t

Fig. 16 shows the effect of t on the flow-fields of the inlets. Fig. 16 (a), (c), (e) and (g) show the schlieren images, while Fig. 16 (b), (d), (f) and (h) shows the Mach contours around flow separation. When $t = 0.3\delta$, SW_1 and SW_3 interact and generate SW_4, as shown in Fig. 16 (a). The separation bubble induced by SW_4 nearly equals that in the baseline inlet, as shown in Fig. 16 (b), which means the BFS is ineffective. When the $t \geq 0.8\delta$, SW_1 and SW_3 impinge on the flat plate, respectively, and the separation bubble is

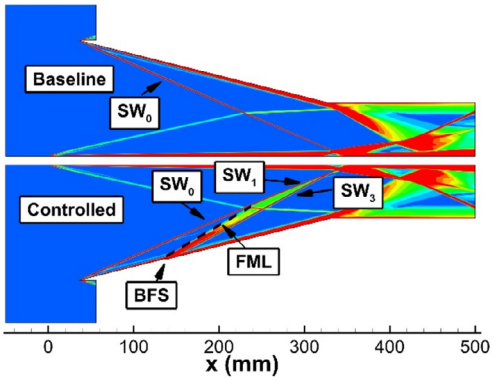

(a) Schlieren image when t=0.3δ

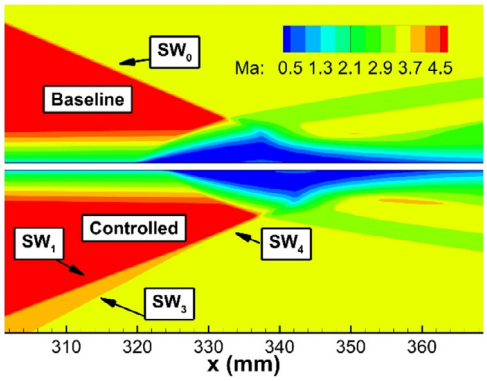

(b) Mach contours when t=0.3δ

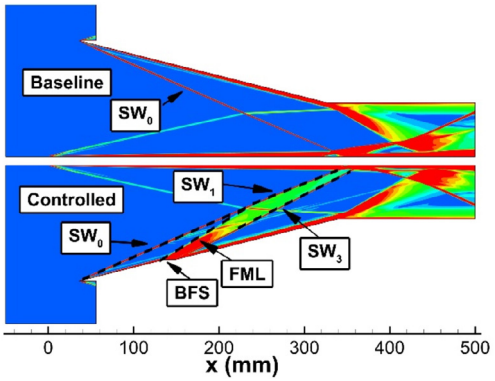

(c) Schlieren image when t=0.8δ

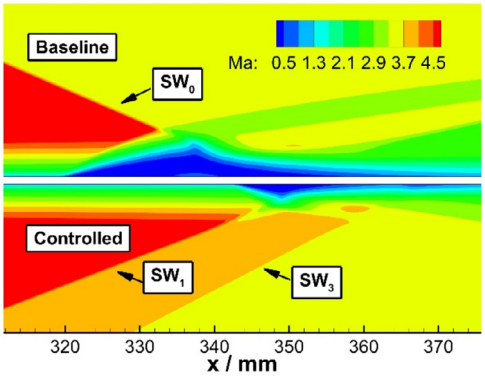

(d) Mach contours when t=0.8δ

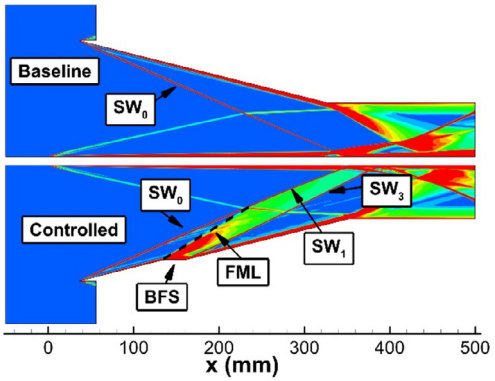

(e) Schlieren image when t=1.6δ

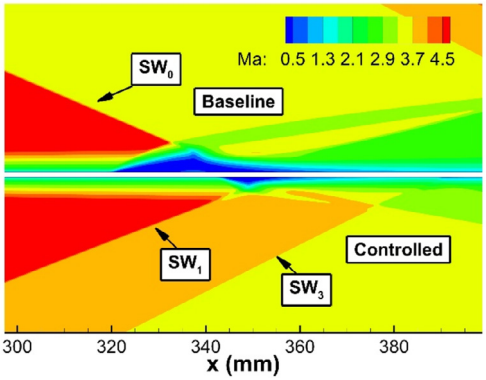

(f) Mach contours when t=1.6δ

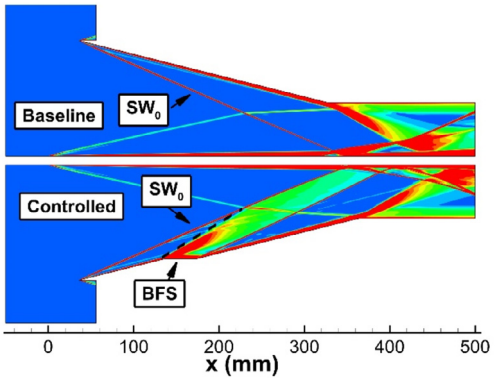

(g) Schlieren image when t=2.4δ

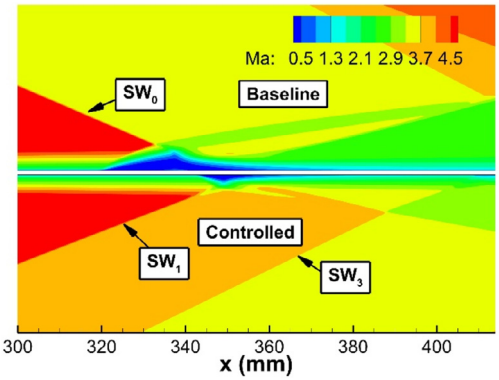

(h) Mach contours when t=2.4δ

Fig. 16. Effect of t on the flow-fields of the inlets.

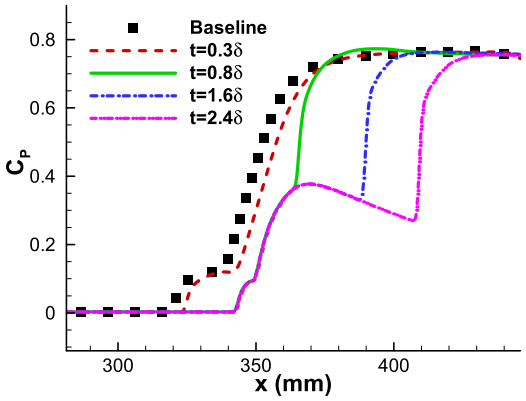

Fig. 17. Effect of t on the pressure coefficient distribution on the flat plate.

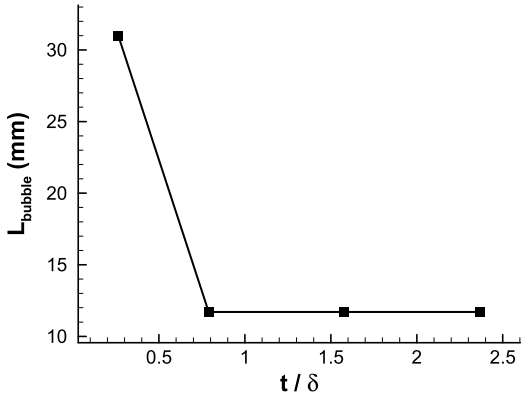

Fig. 18. Effect of t on the length of the separation bubble.

much smaller than that in the baseline inlet, which means the BFS is effective. Besides, although the impingement position of SW_3 moves downstream with increasing t, SW_3 does not induce flow separation.

Fig. 17 shows the effect of t on the pressure coefficient distribution on the flat plate. When $t = 0.3\delta$, the pressure coefficient distribution in the controlled inlet is similar to that in the baseline inlet. It indicates that the BFS is ineffective. When $t \geq 0.8\delta$, the separation point moves downstream significantly, and the pressure coefficient distributions are identical before $x = 364$ mm. After that, when $t = 0.8\delta$, the pressure coefficient increases. However, when $t = 1.6$ and 2.4δ, the pressure coefficient decreases firstly and then increases because the impingement position of SW_3 moves downstream with increasing t.

Fig. 18 shows the effect of t on the length of the separation bubble. When $t = 0.3\delta$, the separation bubble is very large. It indicates that the BFS is ineffective. When $t \geq 0.8\delta$, the length of the separation bubble decreases significantly and is constant with t. In conclusion, the BFS is effective when the thickness is large enough.

4.3.3. Deflection angle, θ

Fig. 19 shows the effect of θ on flow-fields of the inlets. Fig. 19 (a), (c), (e), (g) and (i) show the schlieren images, while Fig. 19 (b), (d), (f), (h) and (j) shows the Mach contours around flow separation. When $\theta = 3$ deg, the separation bubble in the controlled inlet is smaller than that in the baseline inlet, which means the BFS with a small θ can control SWBLI. When $\theta \geq 14$ deg, the separation bubble becomes much smaller. It indicates that the BFS can give full play to the control effect when θ is large enough. However, when θ is very large, the boundary-layer downstream of the BFS separate, as shown in Fig. 20. Flow separation increases the drag, so θ should not be too large.

Fig. 21 shows the effect of θ on the pressure coefficient distribution on the flat plate. The results suggest that the separation point moves downstream with increasing θ. When $\theta \geq 14$ deg, the separation points coincide with each other. Besides, the pressure jump induced by SW_3 moves upstream because the impingement position of SW_3 moves upstream with increasing θ.

Fig. 22 shows the effect of θ on the length of the separation bubble. The length of the separation bubble decreases with increasing θ. However, when $\theta \geq 14$ deg, it is almost a constant, which means the control ability will not enhance when θ is large enough.

4.3.4. Discussion

According to the results of the parameter study, the wave system in the inlet can be classified into three types: effective state, ineffective states, and critical states.

1) Effective state: if the wave system is the same as shown in Fig. 23, the BFS can effectively control flow separation induced by SWBLI. This wave system has two characteristics. The first is that FML interacts with SW_0 and generates SW_1. The second is that SW_1 and SW_3 should not interact. Only the wave system with the above characteristics can replace the strong shock-wave to be weak ones and alleviates flow separation as the purpose.
2) Ineffective states: there are two ineffective states, as shown in Fig. 24. In ineffective state 1, FML does not interact with SW_0. So, the expansion waves cannot weak SW_0. Consequently, the separation bubble cannot become smaller. This state shows up

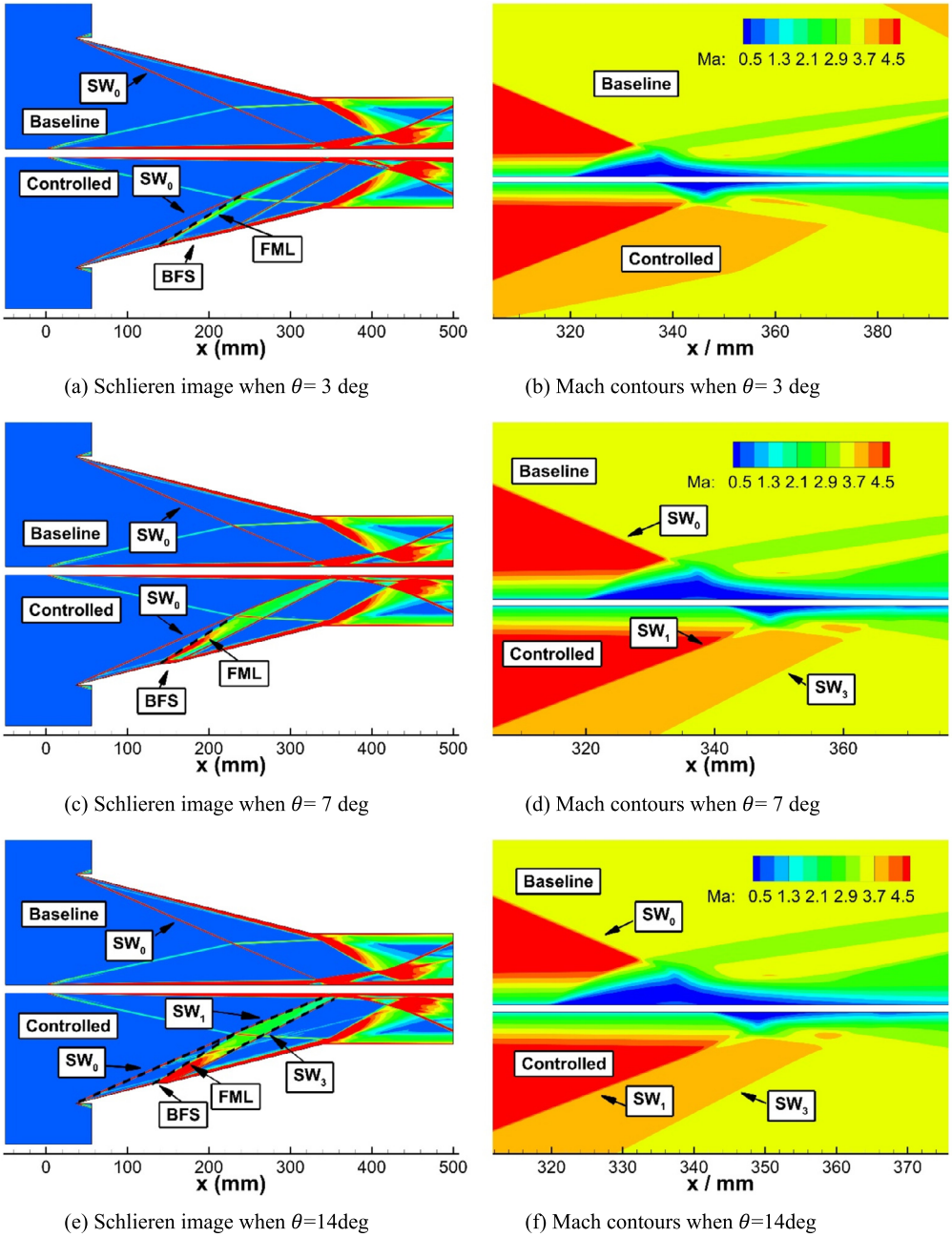

(a) Schlieren image when θ= 3 deg

(b) Mach contours when θ= 3 deg

(c) Schlieren image when θ= 7 deg

(d) Mach contours when θ= 7 deg

(e) Schlieren image when θ=14deg

(f) Mach contours when θ=14deg

Fig. 19. Effect of θ on flow-fields of the inlets.

when L is too large. In ineffective state 2, SW_1 and SW_3 interact and generate SW_4. The pressure jump induced by SW_4 is nearly the same as that induced by SW_0. Hence, the separation bubble also cannot become smaller. This state shows up when L or t is too small.

3) Critical states: there are two critical states, as shown in Fig. 25. In critical state 1, FML interacts with SW_0, and their intersection point is on the flat plate. In critical state 2, the intersection point of SW_1 and SW_3 is on the flat plate.

5. Conclusions

This paper develops a new method to control the shock-wave/boundary-layer interaction in the hypersonic inlet using a backward-facing step. The backward-facing step is fixed on the shock-wave generator. The control effect is verified on a simple inlet at a Mach number of 5. The conclusions obtained from the numerical results are shown as follows.

1) The backward-facing step fixed on the shock-wave generator has a better control effect than that fixed on the flat plate. The results show that the length, height, and volume of the separation bubble are reduced by 62.5%, 72.7%, and 90% in control of the backward-facing step, corresponding parameters are $L = 26\delta$, $\theta = 14$ deg, $t = 0.8\delta$.
2) The control mechanism is that the expansion waves generated by the backward-facing step weak the strong shock-wave brought out by the shock-wave generator. As a result, the strong shock-wave becomes two weak ones. So, the shock-wave/boundary-layer interaction is suppressed.
3) The wave system in the controlled inlet can be classified into three types: effective state, ineffective states, and criti-

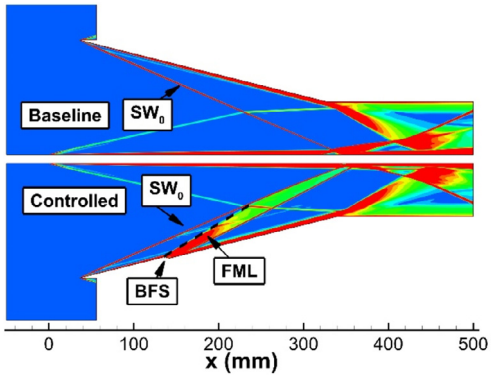

(g) Schlieren image when θ= 30 deg

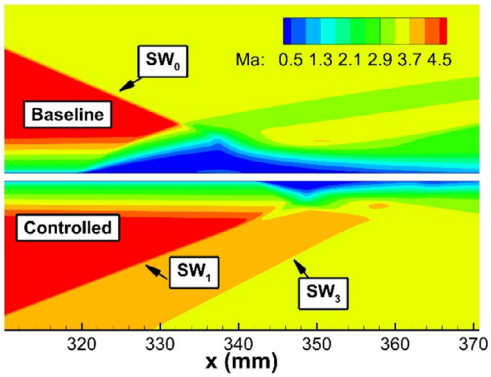

(h) Mach contours when θ= 30 deg

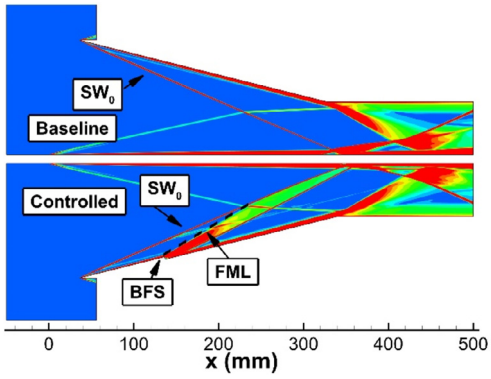

(i) Schlieren image when θ= 90 deg

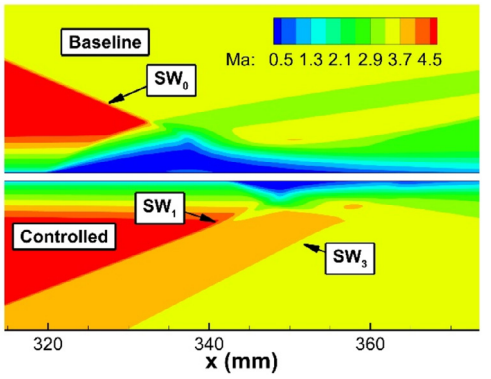

(j) Mach contours when θ= 90 deg

Fig. 19. (*continued*)

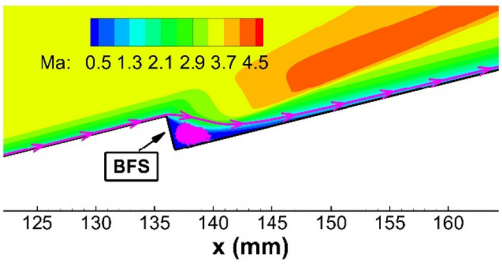

Fig. 20. Flow-field around the BFS when $\theta = 90$ deg.

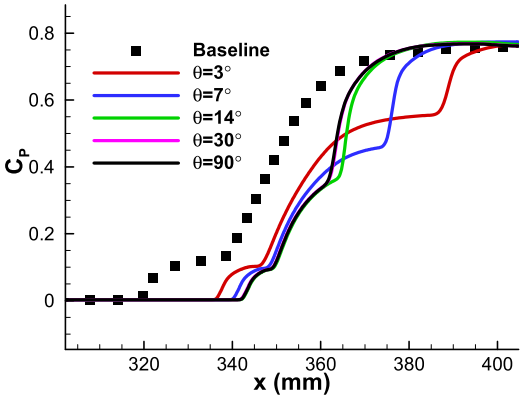

Fig. 21. Effect of θ on the pressure coefficient distribution on the flat plate.

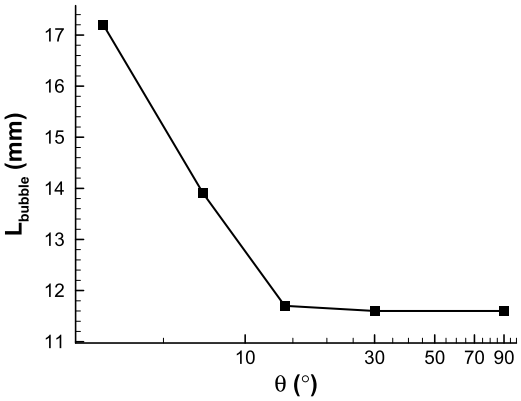

Fig. 22. Effect of θ on the length of the separation bubble.

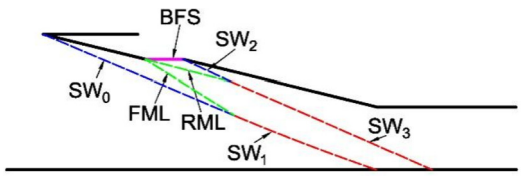

Fig. 23. Wave system of effective state.

cal states. Only when the wave system is in the effective state, the shock-wave/boundary-layer interaction can be suppressed.

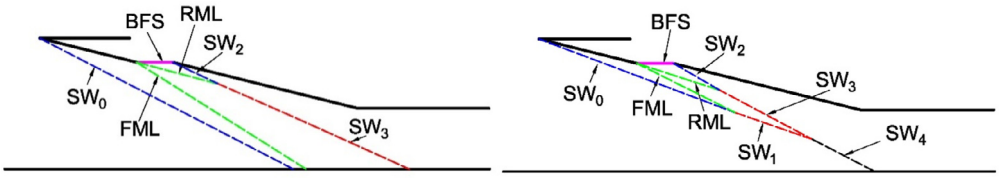

(a) State 1 (b) State 2

Fig. 24. Wave system of ineffective states.

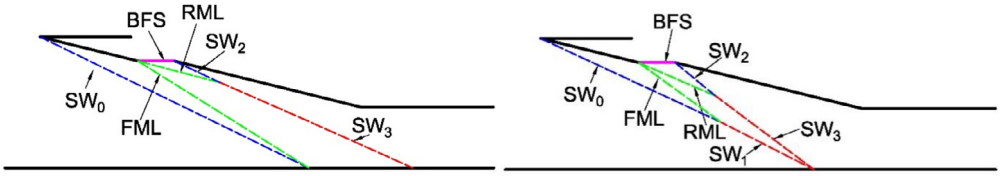

(a) State 1 (b) State 2

Fig. 25. Wave system of critical states.

Declaration of competing interest

The authors declare that they have no known competing financial interests or personal relationships that could have appeared to influence the work reported in this paper.

Acknowledgements

This research did not receive any specific grant from funding agencies in the public, commercial, or not-for-profit sectors.

References

[1] D.Q. Xu, S.B. Luo, J.W. Song, et al., Direct numerical simulations of supersonic compression-expansion slope with a multi-GPU parallel algorithm, Acta Astronaut. 179 (2021) 20–32.
[2] K. Zhu, L.X. Jiang, W.D. Liu, et al., Wall temperature effects on shock wave/turbulent boundary layer interaction via direct numerical simulation, Acta Astronaut. 178 (2021) 499–510.
[3] S. Padmanabhan, J.C. Maldonado, J. Threadgill, et al., Experimental study of swept impinging oblique shock/boundary-layer interactions, AIAA J. 59 (2020) 140–149.
[4] G.M.D. Currao, L.P. Mcquellin, A.J. Neely, et al., Hypersonic oscillating shock-wave/boundary-layer interaction on a flat plate, AIAA J. 59 (2021) 940–959.
[5] W.B. Hu, S. Hickel, B.W. Oudheusden, Low-frequency unsteadiness mechanisms in shock wave/turbulent boundary layer interactions over a backward-facing step, J. Fluid Mech. 915 (2021) A107.
[6] S.K. Im, H. Do, Unstart phenomena induced by flow choking in scramjet inlet-isolators, Prog. Aerosp. Sci. 97 (2018) 1–21.
[7] H.K. Liu, C. Yan, Y. Zhao, et al., Active control method for restart performances of hypersonic inlets based on energy addition, Aerosp. Sci. Technol. 85 (2019) 481–494.
[8] L.J. Yue, Y.N. Jia, X. Xu, et al., Effect of cowl shock on restart characteristics of simple ramp type hypersonic inlets with thin boundary layers, Aerosp. Sci. Technol. 74 (2018) 72–80.
[9] K. Kang, L. Wermer, S. Im, et al., Fast-acting boundary-layer suction to control unstarting and unstarted flows, AIAA J. 58 (2020) 2475–2485.
[10] M.K. Devaraj, P. Jutur, S. Rao, et al., Experimental investigation of unstart dynamics driven by subsonic spillage in a hypersonic scramjet intake at Mach 6, Phys. Fluids 32 (2020) 026103.
[11] M.R. Soltani, A. Daliri, J.S. Younsi, et al., Effects of bleed position on the stability of a supersonic inlet, J. Propuls. Power 32 (2016) 1153–1166.
[12] T.L. Huang, L.J. Yue, X.Y. Chang, Numerical study of a fully confined supersonic slot impinging jet from bleed system, Aerosp. Sci. Technol. 90 (2019) 12–22.
[13] Y.B. He, H.Y. Huang, D.R. Yu, Investigation of corner separation and suction control in constant area duct, Aerosp. Sci. Technol. 66 (2017) 70–82.
[14] H.X. Zhang, S.W. Chen, Q.H. Meng, et al., Flow separation control using unsteady pulsed suction through endwall bleeding holes in a highly loaded compressor cascade, Aerosp. Sci. Technol. 72 (2018) 455–464.
[15] Z.A. Wang, J.T. Chang, Y.F. Li, et al., Investigation of shock wave control by suction in a supersonic cascade, Aerosp. Sci. Technol. 108 (2021) 106382.
[16] J.S. Zhang, H.C. Yuan, Y.F. Wang, et al., Experiment and numerical investigation of flow control on a supersonic inlet diffuser, Aerosp. Sci. Technol. 106 (2020) 106182.
[17] J. Sepahi-Younsi, B. Forouzi Feshalami, S.R. Maadi, R.Z. Mohammad, Boundary layer suction for high-speed air intakes: a review, Proc. Inst. Mech. Eng., G J. Aerosp. Eng. 233 (2019) 3459–3481.
[18] Y. Zhang, H.J. Tan, M.C. Du, et al., Control of shock/boundary-layer interaction for hypersonic inlets by highly swept microramps, J. Propuls. Power 31 (2015) 113–143.
[19] A.G. Panaras, F.K. Lu, Micro-vortex generators for shock-wave/boundary-layer interactions, Prog. Aerosp. Sci. 74 (2015) 16–47.
[20] R. Szwaba, P. Kaczynski, P. Doerffer, Roughness effect on shock wave boundary layer interaction area in compressor fan blades passage, Aerosp. Sci. Technol. 85 (2019) 171–179.
[21] S.B. Verma, C. Manisankar, Control of incident shock-induced separation using vane-type vortex-generating devices, AIAA J. 56 (2018) 1600–1615.
[22] W.Z. Gao, J. Chen, C.H. Liu, et al., Effects of vortex generators on unsteady unstarted flows of an axisymmetric inlet with nose bluntness, Aerosp. Sci. Technol. 104 (2020) 106021.
[23] D.P. Ramaswamy, A.M. Schreyer, Control of shock-induced separation of a turbulent boundary layer using air-jet vortex generators, AIAA J. 59 (2021) 927–939.
[24] B. Hadi, M. Seyed Ali Agha, O. Seyed Amir Abbas, et al., Effects of micro-vortex generators on shock wave structure in a low aspect ratio duct, numerical investigation, Acta Astronaut. 178 (2021) 616–624.
[25] D. Sun, J.Q. Chen, C. Li, et al., On the wake structure of a micro-ramp vortex generator in hypersonic flow, Phys. Fluids 32 (2020) 126111.
[26] J.T. Chang, N. Li, K.J. Xu, et al., Recent research progress on unstart mechanism, detection and control of hypersonic inlet, Prog. Aerosp. Sci. 89 (2017) 1–22.
[27] W. Huang, H. Wu, Y.G. Yang, et al., Recent advances in the shock wave/boundary layer interaction and its control in internal and external flows, Acta Astronaut. 174 (2020) 103–122.
[28] W.P. Li, H. Liu, Large-eddy simulation of shock-wave/boundary-layer interaction control using a backward facing step, Aerosp. Sci. Technol. 84 (2019) 1011–1019.
[29] M.G. Scherberg, H.E. Smith, An experimental study of supersonic flow over a rearward-facing step, AIAA J. 5 (1) (1967) 51–56.
[30] S.Y. Yang, Adaptive analysis of the inviscid supersonic flow over a backward-facing step, J. Propuls. Power 17 (4) (2001) 938–940.
[31] R. Hillier, Shock-wave/expansion-wave interactions and the transition between regular and Mach reflection, J. Fluid Mech. 575 (2007) 399–424.
[32] E. Montazer, H. Yarmand, E. Salami, et al., A brief review study of flow phenomena over a backward-facing step and its optimization, Renew. Sustain. Energy Rev. 82 (2018) 994–1005.
[33] W. Hu, S. Hickel, B.W.V. Oudheusden, Low-frequency unsteadiness mechanisms in shock wave/turbulent boundary layer interactions over a backward-facing step, J. Fluid Mech. 915 (2021) 1–34.
[34] E. Schülein, Skin friction and heat flux measurements in shock/boundary layer interaction flows, AIAA J. 44 (2006) 1732–1741.
[35] J.D. Anderson, Fundamentals of Aerodynamics, 5th edition, Tata McGraw-Hill Education, New York, 2010.
[36] A. Jameson, S. Yoon, Lower-upper implicit schemes with multiple grids for the Euler equations, AIAA J. 25 (1987) 929–935.

[37] P.L. Roe, Approximate Riemann solvers, parameter vectors, and difference schemes, J. Comput. Phys. 43 (1981) 357–372.
[38] B. Van Leer, Towards the ultimate conservative difference scheme, J. Comput. Phys. 135 (1997) 229–248.
[39] F.R. Menter, Two-equation eddy-viscosity turbulence models for engineering applications, AIAA J. 32 (1994) 1598–1605.
[40] W.Z. Xie, Z.M. Wu, A.Y. Yu, et al., Control of severe shock-wave/boundary-layer interactions in hypersonic inlets, J. Propuls. Power 34 (2018) 614–623.
[41] K.K. Yu, J.L. Xu, S. Liu, et al., Starting characteristics and phenomenon of a supersonic wind tunnel coupled with inlet model, Aerosp. Sci. Technol. 77 (2018) 626–637.
[42] L.J. Souverein, P.G. Bakker, P. Dupont, A scaling analysis for turbulent shock-wave/boundary-layer interactions, J. Fluid Mech. 714 (2013) 505–535.